International Journal of Pressure Vessels and Piping 188 (2020) 104211

Contents lists available at ScienceDirect

International Journal of Pressure Vessels and Piping

journal homepage: http://www.elsevier.com/locate/ijpvp

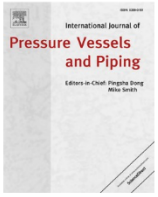

Nonlinear stress and deformation analysis of pressurized thick-walled hyperelastic cylinders with experimental verifications and material identifications

M. Shariyat *, M. Khosravi, M. Yazdani Ariatapeh, M. Najafipour

Faculty of Mechanical Engineering, K.N. Toosi University of Technology, Tehran, 19991-43344, Iran

ARTICLE INFO

Keywords:
Direct hyperelasticity
Neo-hookean and Mooney-Rivlin models
Stress analysis
Thick cylindrical pressure vessels and piping
Experimental verifications

ABSTRACT

The main purpose of the present research is the investigation of the stress and displacement distributions of the internally pressurized thick-walled hyperelastic cylindrical vessels or pressure pipes. The governing equations are derived by incorporation of the incompressible neo-Hookean and Mooney-Rivlin hyperelastic constitutive models into the direct hyperelasticity theory in the von Karman framework of large deformations. In contrast to all the available researches, no simplifications or linearization are made. The non-linear governing equations are solved by utilizing a second-order point-collocation procedure and implementation of details of the proposed incremental iterative solution scheme in the Matlab code written by the authors. Another novelty of the present research is experimentally identifying the employed polymeric hyperelastic material and verification of the results through experiments conducted by the authors. Due to using both nonlinear constitutive laws and nonlinear stress-displacement relations, through-thickness distributions of the radial displacement and radial and circumferential stresses are extracted for various pressures. The experimental results reveal that while the neo-Hookean hyperelastic model cannot be used for materials with stress-softening, the Mooney-Rivlin model reproduces the experimental results with excellent accuracy. In addition to the experimental verification, the results are verified by the Abaqus finite element analysis code as well.

1. Introduction

Hyperelastic materials constitute a material category that includes a huge number of the natural and engineering substances that exhibit large but recoverable deformations with almost no volumetric changes, highly nonlinear behaviors, and higher durability in repetitive deformations. In contrast to other common materials, the stress components of the hyperelastic materials are related to higher powers of the strain components as well [1,2]. The bio-tissues/bio-sensors [3] and plant-tissues (such as wood), polymeric components [4], and adhesives are among the hyperelastic materials that are extensively used in biomechanical, agricultural, vehicular, aeronautic, petrochemical, and other industries. For this reason, numerous researchers have focused on behavior analysis of structures made of these materials, in the recent years [5–7].

The extremely thin hyperelastic shells may successfully be modeled by membranes [8,9]. Hyperelastic thin-walled cylindrical shells with bending stiffness were treated by some researchers. Basar and Ding [10,11] accomplished finite-element deflection, stretch, and stress analyses of the incompressible neo-Hookean and Mooney-Rivlin hyperelastic shells, neglecting the influence of the transverse shear strains. Kiendl et al. [12] analyzed the static behavior of the neo-Hookean hyperelastic thin classical shells based on linearized 3D constitutive models and a linearized incremental solution, enforcing the incompressibility and zero transverse normal stress conditions. Luo et al. [13] performed a static/buckling analysis for the thin classical neo-Hookean and Mooney-Rivlin shells. Breslavsky et a [14]. Studied the static and dynamic responses of a circular cylindrical shell made of neo-Hookean-Fung hyperelastic materials, using a third-order shell theory and strain-energy-density-based Lagrange equations. Amabili et al. [15] employed linearized relations and a higher-order geometrically nonlinear shell theory and imposed the incompressibility condition at the mid-surface of the neo-Hookean hyperelastic transversely flexible cylindrical shell. Zhang et al. [16] studied nonlinear vibration of

* Corresponding author.
E-mail addresses: shariyat@kntu.ac.ir (M. Shariyat), m.khosravi@email.kntu.ac.ir (M. Khosravi), yazdaniaria@email.kntu.ac.ir (M. Yazdani Ariatapeh), najafipour_m@kntu.ac.ir (M. Najafipour).

https://doi.org/10.1016/j.ijpvp.2020.104211
Received 29 March 2020; Received in revised form 25 August 2020; Accepted 31 August 2020
Available online 4 September 2020
0308-0161/

incompressible Mooney-Rivlin thin-walled cylindrical shells under harmonic pressures, employing the small strain hypothesis, incompressibility condition, Lagrange equations of motion, and a simplified trigonometric series solution. Nonlinear frequencies of an incompressible hyperelastic tube surrounded by a nonlinear foundation were studied by Mirjavadi et al. [17]. Fundamental frequency-pressure and pressure-stretch analyses of an incompressible damaged Ogden material pressurized cylindrical tube were presented by Arya et al. [18], using the displacement form of the elasticity equations.

Some authors have studied the thin hyperelastic shells based on the elasticity equations instead of the approximate shell theories. Roussos et al. [19] utilized the stress-based elasticity equations for time variations analysis of the inner radius of the internally pressurized thin-walled incompressible Mooney–Rivlin/neo-Hookean spherical shells. According to the same bases, variations of the hydrostatic pressure rather than the displacements or stresses of neo-Hookean thin cylindrical shells subject dynamic internal pressures were studied by Ren [20] by using stress-based elasticity equations.

Fewer articles have treated thick-walled hyperelastic vessels. Batra and Bahrami [21] studied axisymmetric static stresses of a circular heterogeneous Mooney-Rivlin cylinder whose two material parameters varied through the thickness according to either a power law or affine relations. A plane-strain stress-based formulation and the incompressibility condition were used. By employing an exponential strain energy density and decomposition of the deformation gradient into mechanical and thermal components, Almasi et al. [22] investigated the axisymmetric thermal stresses of the thick incompressible hyperelastic non-pressurized rotating cylinders, under known constant values of the axial and circumferential stretches. Stress-based elasticity formulation was used. Later, Almasi et al. [23] used the same techniques and assumptions to investigate the thermomechanical behaviors of the non-pressurized rotating hyperelastic cylinders. However, the transverse variations of the material properties and their radial derivatives were not described or appeared in the formulation. Aranda-Iglesias et al. [24] investigated the Poincaré maps and Lyapunov exponents of large-amplitude free vibration of an incompressible orthotropic hyperelastic cylinder modeled based on physically-based invariants and finite-deformation Cosserat's membrane theory which permits axial displacement. Ghadiri Rad et al. [25] investigated the nonlinear dynamic behavior of a thick neo-Hooken hyperelastic pressurized cylinder. The Galerkin incremental form of the elasticity equations and the Newmark/Newton-Raphson technique were employed. However, values of the material constants, their radial variations, and their derivatives were not described or appeared explicitly in the governing equations. Bagheri et al. [26] focused on stress distribution and angular velocity-stretch behavior of rotating thick-walled non-pressurized rubberlike cylinders, utilizing known constant stretch values. An Ogden-type model with integer powers and the generalized plane-strain assumption was adopted.

The current article is concerned with stress and displacement distribution investigations of the internally pressurized thick-walled hyperelastic cylindrical pressure vessels/pipes. Some of the novelties/superiorities of the present research may be listed as follows:

- It is the first time that the *direct theory of hyperelasticity* is used to accurately investigate the stress and deformations of the pressurized hyperelastic cylinders. The previous researches either have treated non-pressurized cylinders or used the approximate shell theories.
- Both large deformation and material nonlinearities are considered. No simplifications or linearization are made in the resulting equations.
- In contrast to previous researches that either imposed known fixed stretches or presented stress-based formulations, both the displacement and stress components are extracted.
- To present realistic results, the employed material properties are identified based on matching the hyperelastic models to the stress-stretch curves found experimentally by the authors.
- The analysis results are verified by the experimental results of the authors and the Abaqus results.
- The non-linear governing equations are solved by a second-order point collocation method and implementation of an incremental iterative solution scheme in the Matlab code written by the authors rather than using the commercial computer codes. The proposed point collocation procedure overcomes some shortcomings of the commercial finite element analysis codes, such as ANSYS, Abaqus, and NASTRAN, in addition to using quite different theoretical bases.

The governing equations are developed based on the displacement-based version of the *direct hyperelasticity theory* of elasticity. von Karman's large deformation framework is incorporated in the development of the hyperelastic implicit strain-displacement equations. The incompressible neo-Hookean and Mooney-Rivlin hyperelastic constitutive models are employed and the governing equations are solved based on a second-order point-collocation technique. Due to using both nonlinear constitutive laws and nonlinear stress-displacement relations, through-thickness distributions of the radial displacement and radial and circumferential stresses are extracted for various pressures. Moreover, the results are verified by both the Abaqus and experimental results.

2. The theoretical background for determination of the stress components

Unlike the traditional elastic materials, the stresses of the hyperelastic materials cannot be directly related to the strain components. Instead, the stress components may be related to the derivatives of the strain energy density in terms of the displacement components/derivatives. The constitutive law of a hyperelastic material may be derived from an equation relating the strain energy density of the material to the deformation gradient or equivalently, the invariants of the strain tensor:

$$W(\boldsymbol{F}) = W(I_1, I_2, I_3) = \overline{W}\left(\bar{I}_1, \bar{I}_2, J\right) \tag{1}$$

where $\boldsymbol{F}$and J are the deformation gradient vector and Jacobian of the transformation from the initial to the deformed configuration:

$$F_{ij} = \frac{\partial x_i}{\partial X_j} = \delta_{ij} + \frac{\partial u_i}{\partial X_j}, \quad J = |\boldsymbol{F}| \tag{2}$$

δ_{ij} is Kronecker's delta symbol, X_j and x_i are respectively, coordinates of the particle in the original and deformed configurations, and I_1, I_2, I_3 are invariants of the left Cauchy-Green deformation tensor $\boldsymbol{B}$:

$$\boldsymbol{B} = \boldsymbol{F}.\boldsymbol{F}^{\boldsymbol{T}}; B_{ij} = F_{ik}F_{jk} + \frac{\partial u_i}{\partial x_j} \tag{3}$$

$$I_1 = trace\ (\boldsymbol{B}) = B_{kk}, \quad I_2 = \frac{1}{2}\left(I_1^2 - \boldsymbol{B}...\boldsymbol{B}\right) = \frac{1}{2}\left(I_1^2 - B_{ik}B_{ki}\right), \quad I_3 = |\boldsymbol{B}| = J^2 \tag{4}$$

u_i are displacements of the particles due to the resulting deformations.

For nearly incompressible materials, the following invariants of **B** that do not change under pure volume change have been proposed [6]:

$$\bar{I}_1 = \frac{I_1}{J^{2/3}} = \frac{B_{kk}}{J^{2/3}}, \quad \bar{I}_2 = \frac{I_2}{J^{4/3}} = \frac{1}{2}\left(\bar{I}_1^2 - \frac{B_{ik}B_{ki}}{J^{4/3}}\right), \quad J = \sqrt{|\boldsymbol{B}|} \tag{5}$$

The first Piola-Kirchhoff (S_{ij}) stress components can be extracted from the differentiation of the strain energy density

$$S_{ij} = \frac{\partial W}{\partial F_{ji}} \tag{6}$$

In turn, the actual stress components, namely Cauchy's (σ_{ij}) stress

components, may be related to the definition of the nominal stress as follows [6].

$$\sigma_{ij}=\frac{F_{ik}}{J}S_{kj}=\frac{F_{ik}}{J}\frac{\partial W}{\partial F_{jk}} \tag{7}$$

For a nearly incompressible isotropic material, applying the chain rule to Eq. (1) in terms of the alternative set of the invariants of the left Cauchy-Green deformation tensor yields

$$\frac{\partial W}{\partial F_{ij}}=\frac{\partial \overline{W}}{\partial \overline{I}_1}\frac{\partial \overline{I}_1}{\partial F_{ij}}+\frac{\partial \overline{W}}{\partial \overline{I}_2}\frac{\partial \overline{I}_2}{\partial F_{ij}}+\frac{\partial \overline{W}}{\partial J}\frac{\partial J}{\partial F_{ij}} \tag{8}$$

So, based on the identities defined in Eq. (5) one has

$$\frac{\partial J}{\partial F_{ij}}=JF^{-1}_{ji},\quad \frac{\partial \overline{I}_1}{\partial F_{ij}}=\frac{2}{J^{2/3}}F_{ij}-\frac{2}{3}\overline{I}_1F^{-1}_{ji},\quad \frac{\partial \overline{I}_2}{\partial F_{ij}}$$
$$=\frac{2}{J^{\frac{2}{3}}}\overline{I}_1F_{ij}-\frac{2}{J^{\frac{4}{3}}}B_{ik}F_{kj}-\frac{4\overline{I}_2}{3}\overline{I}_1F^{-1}_{ji} \tag{9}$$

The true stress components can be obtained by substituting Eqs. (8) and (9) into Eq. (7) as

$$\sigma_{ij}=\frac{2}{J^{5/3}}\left(\frac{\partial \overline{W}}{\partial \overline{I}_1}+\overline{I}_1\frac{\partial \overline{W}}{\partial \overline{I}_2}\right)B_{ij}-\frac{2}{3J}\left(\overline{I}_1\frac{\partial \overline{W}}{\partial \overline{I}_1}+2\overline{I}_2\frac{\partial \overline{W}}{\partial \overline{I}_2}\right)\delta_{ij}-\frac{2}{J^{\frac{7}{3}}}\frac{\partial \overline{W}}{\partial \overline{I}_2}B_{ik}B_{kj}+\frac{\partial \overline{W}}{\partial J}\delta_{ij} \tag{10}$$

For a generalized Neo-Hookean solid model, the following strain energy density function may be assigned [6].

$$\overline{W}=\frac{\mu_1}{2}\left(\overline{I}_1-3\right)+\frac{K_1}{2}(J-1)^2 \tag{11}$$

μ_1 and K_1 are material properties that are respectively, the shear and bulk moduli for small deformations. Eq. (24) corresponds to a nearly incompressible material where $K_1\gg\mu_1$. The relevant stress components can be determined based on Eq. (10)

$$\sigma_{ij}=\frac{\mu_1}{J^{5/3}}\left(B_{ij}-\frac{1}{3}B_{kk}\delta_{ij}\right)+K_1(J-1)\delta_{ij},\ i,j=1,2,3 \tag{12}$$

On the other hand, the strain energy density function associated with the generalized Mooney-Rivlin solid is

$$\overline{W}=\frac{\mu_1}{2}\overline{I}_1-3\Big)+\frac{\mu_2}{2}\overline{I}_2-3\Big)+\frac{K_1}{2}(J-1)^2 \tag{13}$$

μ_1, μ_1, and K_1 are material properties that can be related to the shear and bulk moduli in small deformations and $\mu=\mu_1+\mu_2$. Eq. (13) should be employed for an almost incompressible material where $K_1\gg\mu_1$. The relevant stress components may be computed from

$$\sigma_{ij}=\frac{\mu_1}{J^{\frac{5}{3}}}\left(B_{ij}-\frac{1}{3}B_{kk}\delta_{ij}\right)+\frac{\mu_2}{J^{\frac{7}{3}}}\left(B_{kk}B_{ij}-\frac{1}{3}(B_{kk})^2\delta_{ij}-B_{ik}B_{kj}+\frac{1}{3}B_{kn}B_{nk}\delta_{ij}\right)$$
$$+K_1(J-1)\delta_{ij},\quad i,j=1,2,3 \tag{14}$$

For fully incompressible materials, the $(J-1)$ expression of Eqs. (12) and (14) becomes zero. But in this case, Eqs. (12) and (14) give the deviatoric stress components only. Because in this case, any arbitrary hydrostatic pressure does not change the volume of the solid. For this reason, an expression containing the hydrostatic pressure has to be added to the normal stress expressions; so that, Eqs. (12) and (14) become

$$\sigma_{ij}=\frac{\mu_1}{J^{5/3}}\left(B_{ij}-\frac{1}{3}B_{kk}\delta_{ij}\right)+\delta_{ij}p\,/\,3,\ i,j=1,2,3 \tag{15}$$

$$\sigma_{ij}=\frac{\mu_1}{J^{\frac{5}{3}}}\left(B_{ij}-\frac{1}{3}B_{kk}\delta_{ij}\right)+\frac{\mu_2}{J^{\frac{7}{3}}}\left(B_{kk}B_{ij}-\frac{1}{3}(B_{kk})^2\delta_{ij}-B_{ik}B_{kj}+\frac{1}{3}B_{kn}B_{nk}\delta_{ij}\right)$$
$$+\delta_{ij}p\,/\,3\delta_{ij},\quad i,j=1,2,3 \tag{16}$$

3. The displacement-based governing equations

The considered long thick-walled cylinder/pipe is fabricated from an incompressible rubberlike material. The inner and outer radii of the cylinder are denoted by a and b, respectively, and the inner and outer boundaries of the vessel are exposed to p_{in} and p_{out} pressures, respectively, as may be seen in Fig. 1. To ascertain the deformation gradient tensor, the coordinates system denoting locations of the particles in the original and deformed coordinates must be defined. These cylindrical coordinates are shown by (R,Θ,Z) and (r,θ,z), respectively. Therefore, the coordinates transformation equations can be written as:

$$r=r(R),\theta=\Theta,z=Z \tag{17}$$

Due to the symmetry, the θ coordinate may be released; so that, by using the plane-strain assumption, the z coordinate may also be ignored. Therefore, as Fig. 1 illustrates, a layer that is originally located at a specific R radial position moves to a new r radial location. It is evident that the difference between these locations indicates the radial displacement

$$r-R=u\ \ \Rightarrow r=R+u \tag{18}$$

According to Eqs. (2) and (18), the deformation gradient tensor becomes

$$\boldsymbol{F}=\begin{pmatrix}\frac{dr}{dR} & 0 & 0\\ 0 & \frac{r}{R} & 0\\ 0 & 0 & 1\end{pmatrix};\quad X_i\equiv R,\quad x_i\equiv r \tag{19}$$

Therefore, based on Eqs. (3) and (19) one has

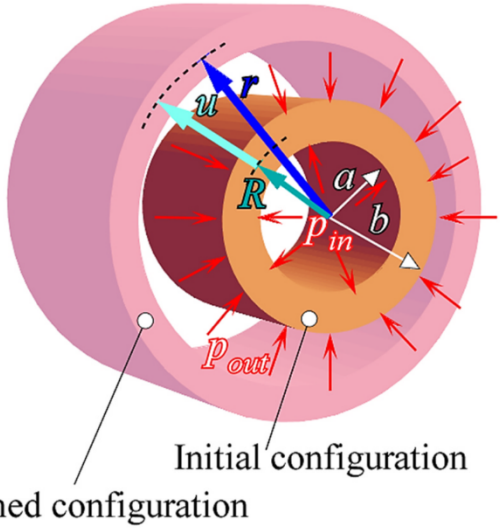

Fig. 1. The original and deformed configurations of the pressurized cylindrical vessel/pipe.

$$\boldsymbol{B}=\boldsymbol{F}.\boldsymbol{F}^{T}=\begin{bmatrix}\left(\frac{dr}{dR}\right)^{2} & 0 & 0\\ 0 & \left(\frac{r}{R}\right)^{2} & 0\\ 0 & 0 & 1\end{bmatrix} \tag{20}$$

So, according to Eq. (18), Eq. (20) may be rewritten as

$$\frac{r}{R}=1+\frac{u}{R},\ dr=dR+du\rightarrow\ \frac{dr}{dR}=\frac{du}{dR}+1 \tag{21}$$

$$\boldsymbol{F}=\begin{pmatrix}1+\frac{du}{dR} & 0 & 0\\ 0 & 1+\frac{u}{R} & 0\\ 0 & 0 & 1\end{pmatrix} \tag{22}$$

$$\boldsymbol{B}=\begin{bmatrix}\left(1+\frac{du}{dR}\right)^{2} & 0 & 0\\ 0 & \left(1+\frac{u}{R}\right)^{2} & 0\\ 0 & 0 & 1\end{bmatrix} \tag{23}$$

The stress components may be expressed in terms of the displacement components; so that, according to Eq. (15) the nonlinear stress components associated with the neo-Hookean model become

$$\sigma_{rr}=\mu_1\left\{\left(1+\frac{du}{dR}\right)^{2}-\frac{1}{3}\left[\left(1+\frac{u}{R}\right)^{2}+\left(1+\frac{du}{dR}\right)^{2}+1\right]\right\}+p/3 \tag{24}$$

$$\sigma_{\theta\theta}=\mu_1\left\{\left(1+\frac{u}{R}\right)^{2}-\frac{1}{3}\left[\left(1+\frac{u}{R}\right)^{2}+\left(1+\frac{du}{dR}\right)^{2}+1\right]\right\}+p/3 \tag{25}$$

and those of the Mooney-Rivlin model take the following form [Eq. (16)]

$$\sigma_{rr}=\sigma_{11}=\mu_1\left[\frac{4}{3}\frac{du}{dR}+\frac{2}{3}\left(\frac{du}{dR}\right)^{2}-\frac{2}{3}\frac{u}{R}-\frac{1}{3}\left(\frac{u}{R}\right)^{2}\right]+\mu_2\left\{\frac{du}{dR}\left[\frac{4}{3}\frac{u}{R}+\frac{2}{3}\left(\frac{u}{R}\right)^{2}+\frac{4}{3}\right]+\left(\frac{du}{dR}\right)^{2}\left[\frac{2}{3}+\frac{2}{3}\frac{u}{R}+\frac{1}{3}\left(\frac{u}{R}\right)^{2}\right]-\frac{2}{3}\frac{u}{R}-\frac{1}{3}\left(\frac{u}{R}\right)^{2}\right\}+p/3 \tag{26}$$

$$\sigma_{\theta\theta}=\sigma_{22}=\mu_1\left[-\frac{2}{3}\frac{du}{dR}-\frac{1}{3}\left(\frac{du}{dR}\right)^{2}+\frac{4}{3}\frac{u}{R}+\frac{2}{3}\left(\frac{u}{R}\right)^{2}\right]+\mu_2\left\{\frac{du}{dR}\left[\frac{4}{3}\frac{u}{R}+\frac{2}{3}\left(\frac{u}{R}\right)^{2}-\frac{2}{3}\right]+\left(\frac{du}{dR}\right)^{2}\left[-\frac{1}{3}+\frac{2}{3}\frac{u}{R}+\frac{1}{3}\left(\frac{u}{R}\right)^{2}\right]+\frac{4}{3}\frac{u}{R}+\frac{2}{3}\left(\frac{u}{R}\right)^{2}\right\}+p/3 \tag{27}$$

Although some references have set the hydrostatic stress p of the stress expressions equal to zero, this assumption leads to incorrect/wrong results. As mentioned before, neglecting this pressure gives the deviatoric stress only and the pressure boundary conditions will be imposed incorrectly. The hydrostatic pressure may be determined after incorporation of the pressure boundary conditions.

The radial equilibrium equations in terms of the stress components in the cylindrical coordinates are

$$\frac{d\sigma_r}{dR}+\frac{\sigma_r-\sigma_\theta}{R}=0 \tag{28}$$

where σ_r and σ_θ are the radial and circumferential stress components, respectively. Substituting Eqs. (24) and (25) into Eq. (28) leads to the neo-Hookean and substituting Eqs. (26) and (27) into Eq. (28) yields the Mooney-Rivlin forms of the radial equilibrium equations in terms of the displacement component:

$$4\frac{d^2u}{dR^2}+\frac{4}{R}\frac{du}{dR}-4\frac{u}{R^2}-2\frac{u}{R^2}\frac{du}{dR}=0 \tag{29}$$

$$\begin{aligned}&\mu_1\left[\frac{4}{3}\frac{d^2u}{dR^2}+\frac{4}{3}\frac{du}{dR}\frac{d^2u}{dR^2}-\frac{2}{3R}\frac{du}{dR}+\frac{2}{3}\frac{u}{R^2}-\frac{2}{3}\frac{u}{R^2}\frac{du}{dR}+\frac{2}{3}\frac{u^2}{R^3}\right]\\&+\mu_2\left[\frac{d^2u}{dR^2}\left(\frac{4}{3}\frac{u}{R}+\frac{2}{3}\left(\frac{u}{R}\right)^{2}+\frac{4}{3}\right)+\frac{du}{dR}\left(\frac{4}{3R}\frac{du}{dR}-\frac{4}{3}\frac{u}{R^2}+\frac{4}{3}\frac{u}{R^2}\frac{du}{dR}-\frac{4}{3}\frac{u^2}{R^3}\right)\right.\\&+2\frac{du}{dR}\frac{d^2u}{dR^2}\left(\frac{2}{3}+\frac{2}{3}\frac{u}{R}+\frac{1}{3}\left(\frac{u}{R}\right)^{2}\right)+\left(\frac{du}{dR}\right)^{2}\left(\frac{2}{3R}\frac{du}{dR}-\frac{2}{3}\frac{u}{R^2}+\frac{2}{3}\frac{u}{R^2}\frac{du}{dR}-\frac{2}{3}\frac{u^2}{R^3}\right)\\&\left.-\frac{2}{3R}\frac{du}{dR}+\frac{2}{3}\frac{u}{R^2}-\frac{2}{3}\frac{u}{R^2}\frac{du}{dR}+\frac{2}{3}\frac{u^2}{R^3}\right]+\mu_1\left[\frac{2}{R}\frac{du}{dR}+\frac{1}{R}\left(\frac{du}{dR}\right)^{2}-2\frac{u}{R^2}-\frac{u^2}{R^3}\right]\\&+\mu_2\left[\frac{2}{R}\frac{du}{dR}+\frac{1}{R}\left(\frac{du}{dR}\right)^{2}-2\frac{u}{R^2}-\frac{u^2}{R^3}\right]=0\end{aligned} \tag{30}$$

For pressurized cylinders, Eqs. (28) and (29) may be solved along with the following boundary conditions:

$$\sigma_r|_{r=a}=-p_{in},\qquad \sigma_r|_{r=b}=-p_{out} \tag{31}$$

where σ_r can be substituted from either Eq. (24) or (26), depending on the employed hyperelastic model, e.g.,

$$\begin{aligned}&\mu_1\left[\frac{4}{3}\frac{du}{dR}\Big|_{R=a}+\frac{2}{3}\left(\frac{du}{dR}\Big|_{R=a}\right)^{2}-\frac{2}{3}\frac{u}{a}-\frac{1}{3}\left(\frac{u}{a}\right)^{2}\right]+\mu_2\left\{\frac{du}{dR}\Big|_{R=a}\left[\frac{4}{3}\frac{u}{a}+\frac{2}{3}\left(\frac{u}{a}\right)^{2}+\frac{4}{3}\right]+\left(\frac{du}{dR}\Big|_{R=a}\right)^{2}\left[\frac{2}{3}+\frac{2}{3}\frac{u}{a}+\frac{1}{3}\left(\frac{u}{a}\right)^{2}\right]-\frac{2}{3}\frac{u}{a}-\frac{1}{3}\left(\frac{u}{a}\right)^{2}\right\}+\frac{p}{3}\\&=-p_{in}\end{aligned} \tag{32}$$

$$\begin{aligned}&\mu_1\left[\frac{4}{3}\frac{du}{dR}\Big|_{R=b}+\frac{2}{3}\left(\frac{du}{dR}\Big|_{R=b}\right)^{2}-\frac{2}{3}\frac{u}{b}-\frac{1}{3}\left(\frac{u}{b}\right)^{2}\right]+\mu_2\left\{\frac{du}{dR}\Big|_{R=b}\left[\frac{4}{3}\frac{u}{b}+\frac{2}{3}\left(\frac{u}{b}\right)^{2}+\frac{4}{3}\right]+\left(\frac{du}{dR}\Big|_{R=b}\right)^{2}\left[\frac{2}{3}+\frac{2}{3}\frac{u}{R}+\frac{1}{3}\left(\frac{u}{b}\right)^{2}\right]-\frac{2}{3}\frac{u}{b}-\frac{1}{3}\left(\frac{u}{b}\right)^{2}\right\}+p/3\\&=-p_{out}\end{aligned} \tag{33}$$

4. The point-collocation solution technique

The governing equations (29) and (30) are nonlinear and thus, cannot be solved analytically. For this reason, it is intended to solve them by a second-order point collocation method. This method is especially suitable for materials with higher deformability/movability, such as polymers and fluids, in addition to accuracy, simplicity, and locking-free nature. For this reason, this approach is the most common procedure that has been implemented in all the computational fluid dynamic (CFD) computer codes. Moreover, the finite element procedure cannot trace the sever changes within the element and consider these changes as errors that must be distributed over the whole domain [27–29], in addition to the stress jumps caused by the Lagrangian elements [27,30,31].

To apply the point collocation technique, the radial domain of the cylinder has to be divided into N segment through defining $N+1$ nodal points. These segments can be of identical lengths, but to capture variations of the quantities more accurately in the vicinity of the inner and outer boundaries where the explicit (pressure-type boundary conditions) or implicit (displacement-based boundary conditions) loads act, it is recommended to use a Chebyshev distribution of the coordinates for the nodal points:

$$R_i=\frac{1}{2}\left[1-cos\frac{(i-1)\pi}{N}\right](b-a)+a;\ i=1,2,3,\cdots,N+1 \tag{34}$$

Using second-order approximations that are equivalent to using second-order Taylor's expansions, implies that the approximation error reduces to one fourth when the distances between the nodal points are

halved.

For the intermediate nodal points, the derivative expressions are discretized according to the central difference scheme, e.g.

$$\left.\frac{du}{dR}\right|_i = \frac{u_{i+1}-u_{i-1}}{2\Delta R}, \left.\frac{d^2u}{dR^2}\right|_i = \frac{u_{i+1}-2u_i+u_{i-1}}{\Delta R^2};\ 2 \le i \le N \tag{35}$$

For the boundary nodal points, either a forward or backward scheme must be used [32–34]:

$$\left.\frac{du}{dR}\right|_i = \begin{cases} \dfrac{-u_2+4u_1-3u_0}{2\Delta R};\ i=0 \\ \dfrac{3u_N-4u_{N-1}+u_{N-2}}{2\Delta R};\ i=N+1 \end{cases} \tag{36}$$

$$\left.\frac{d^2u}{dR^2}\right|_i = \begin{cases} \dfrac{u_2-2u_1+u_0}{\Delta R^2};\ i=0 \\ \dfrac{u_N-2u_{N-1}+u_{N-2}}{\Delta R^2};\ i=N+1 \end{cases} \tag{37}$$

Substituting Eqs. (35)–(37) in either Eq. (29) or (30) for each of the individual nodal points, leads to a nonlinear coupled system of equations that can be described by the following compact form:

$$\boldsymbol{k}_{(N+1)\times(N+1)}\boldsymbol{u}_{(N+1)\times 1} = \boldsymbol{A}_{(N+1)\times 1} \tag{38}$$

To achieve Eq. (38), each nonlinear expression has to be decomposed into two parts where the first part contributes to the formation of the $\boldsymbol{k}$ matrix whereas the second part may be represented by the vector of the nodal unknowns $\boldsymbol{u}$, e.g.,

$$\left[\frac{d^2u}{dR^2}\left(\frac{u}{R}\right)^2\right]_i^{(j)} = \left[\frac{d^2u}{dR^2}\frac{u}{R^2}\right]_i^{(j)} u_i^{(j)} \cong \left[\frac{d^2u}{dR^2}\frac{u}{R^2}\right]_i^{(j-1)} u_i^{(j)} \tag{39}$$

j is the loading step counter. In Eq. (39), the $\frac{d^2u}{dR^2}\frac{u}{R^2}$ expression contributes to the formation of the $\boldsymbol{k}$ matrix. Indeed, the resulting nonlinear system of equations must be solved by using an appropriate incremental iterative solution. In this regard, the final load must be divided into a huge number of loading steps. If it is intended to use an iterative solution technique within each loading step, the first identity of Eq. (39) may be used; so that, the following nonlinear system must be solved iteratively within each loading step

$$\boldsymbol{k}^{(j)}\boldsymbol{u}^{(j)} = \boldsymbol{A}^{(j)} \tag{40}$$

In this connection, $\boldsymbol{k}^{(j-1)}$ may be used as a first guess. The alternative economically more efficient approach relies on the fact that due to the huge number of the loading steps, the difference between $\boldsymbol{k}^{(j)}$ and $\boldsymbol{k}^{(j-1)}$ is negligible; so that, one may use approximations like that of the last identity/approximation of Eq. (39). In other words, the following approximation may be employed:

$$\boldsymbol{k}^{(j-1)}\boldsymbol{u}^{(j)} = \boldsymbol{A}^{(j)} \tag{41}$$

It is crucial to note that the boundary conditions such as those appearing in Eqs. (32) and (33) should be imposed in the resulting coupled nonlinear system, e.g., through employing a penalty method [35], before the solution procedure commences.

5. Results and discussions

As mentioned before, no simplifications or linearization types are employed in the development of the present formulations or extraction of the results. Some of the common simplifications or linearization types (that have not been used here) may be listed as:

- Neglecting the hydrostatic pressure. Therefore, the resulting stress field will be deviatoric rather than the whole stress field.
- Using the small strains assumption.
- Linearizing the resulting final equations, before solution; either by directly omitting the nonlinear terms or replacing the nonlinear terms by simplified series expansions in terms of the displacement components or their derivatives, about a fixed loading condition of a specific layer among the infinite layers of the structure.
- Imposing the incompressibility condition for only one layer.
- Linearizing the inherently nonlinear constitutive law of the hyperelastic material.
- Assuming small deformations.
- Using bilinear/linear elements instead of the bi-quadratic/quadratic elements.
- Neglecting the higher powers of (r/R) or (dr/dR) in comparison to the first powers of these quantitates.
- Neglecting the higher-order derivatives of r with respect to R.
- Approximating the higher powers of (r/R) by unity.
- Assuming a fixed, identical, and known value for the radial/axial stretches of the whole points of the entire cylinder.

Most of these types of linearization lead to wrong formulations and/or results. For this reason, some of the articles on the hyperelastic thick cylinders are excluded from the literature survey section of the current paper.

5.1. The material identification and extraction of the constants of the hyperelastic models

To present realistic results and conclusions, the material properties are extracted experimentally. Furthermore, the results of the written Matlab code are verified experimentally, for the same component, by experiments conducted by the authors of the present article. The chosen component is a flexible clear water hose pipe/tube that is fabricated from a material composition including the thermoplastic PVC (polyvinyl chloride), NBR (acrylonitrile butadiene rubber), and mineral fillers as constituent materials. Due to the symmetry of the loading and boundary conditions, elements of the cylinder are free of radial shear. For this reason, a tensile experiment was performed for the material. To achieve reliable experimental results, the specimen was prepared according to ASTM D638-14. According to this standard manual, type IV specimen shall be used for testing nonrigid plastics whose thickness is 4 mm or less. The thickness and inner radius of the chosen thick-walled tube were 2 mm and 5 mm, respectively. The key dimensions of the test specimen are shown in Fig. 2 and the relevant values are given in Table 1.

The specimen is cut from the tube/hose and flattened before applying the final standard dimension. However, identical results were obtained by using a flat specimen prepared by the supplier. The prepared flat specimen was drawn in the tensile testing machine shown in Fig. 3 at a 4 mm/min rate, at room (25 °C) temperature, until rupture occurred. During the experiment, the initial distance of 25 mm between the grips reached 85 mm. The resulting load histogram reported by the tensile testing machine is shown in Fig. 4. Although the test was

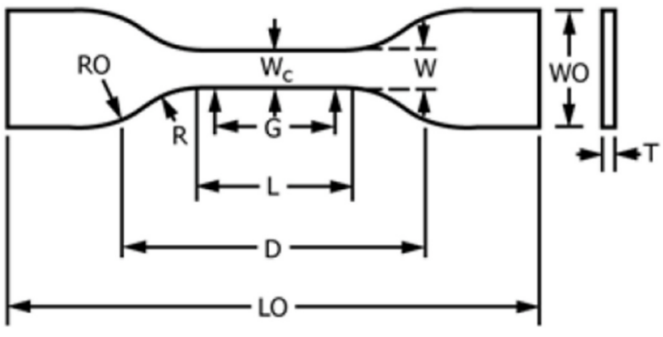

Fig. 2. The key dimensions of the specimen that was prepared according to ASTM D638-14 [36].

Table 1
Values of the dimensions indicated in Fig. 2, according to ASTM D638-14.

Dimension description	Value (mm)
T (Thickness)	2
W (Width of the narrow section)	7
L (Length of the narrow section)	33
WO (Width overall, min)	19
LO (Length overall, min)	115
G (Gage length)	25
D (Distance between grips)	65
R (Radius of fillet)	14
RO (Outer radius)	25

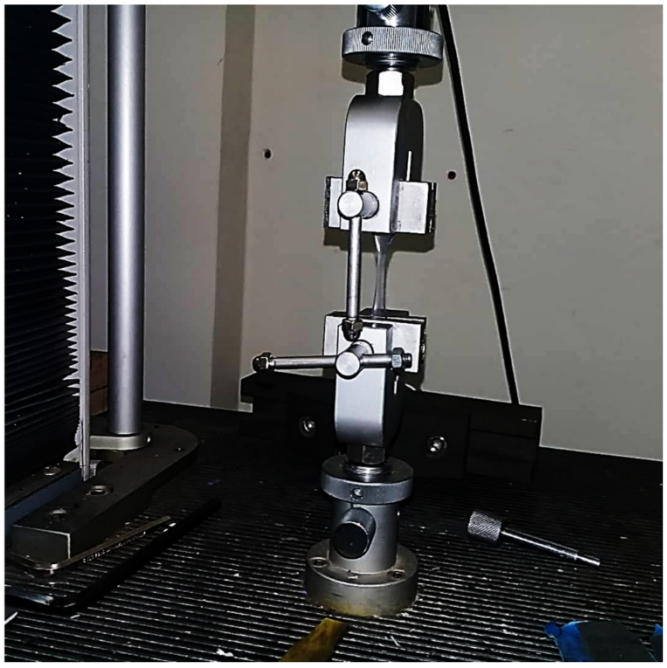

Fig. 3. The employed tensile testing machine and specimen during the testing.

repeated for many specimens, the tensile results obtained for various specimens were almost coincident.

The load-stretch curve associated with the histogram illustrated in Fig. 4 is presented in Fig. 5. The resulting curve demonstrates a degressive stiffness, namely, softening behavior; so that, the slope of the curve and consequently, the tangent modulus of the relevant stress-strain curve decreases with the applied load. It may readily be noted that the material features a nonlinear behavior, even in very small magnitudes of the applied load.

The material constants of the neo-Hookean and Mooney-Rivlin hyperelastic models are extracted based on matching the neo-Hookean and Mooney-Rivlin constitutive laws with the experimental tensile stress-stretch curve [37].

$$\sigma_{neo-Hookean} = 2C_1\left(\lambda^2 - \frac{1}{\lambda}\right) \tag{42}$$

$$\sigma_{Mooney-Rivlin} = 2C_{10}\left(\lambda - \frac{1}{\lambda}\right) + 2C_{01}\left(1 - \frac{1}{\lambda^3}\right) \tag{43}$$

where the stretch λ of the tensile test may be determined from

$$\lambda = \frac{l}{l_0} = 1 + \frac{\Delta l}{l} = 1 + \varepsilon \tag{44}$$

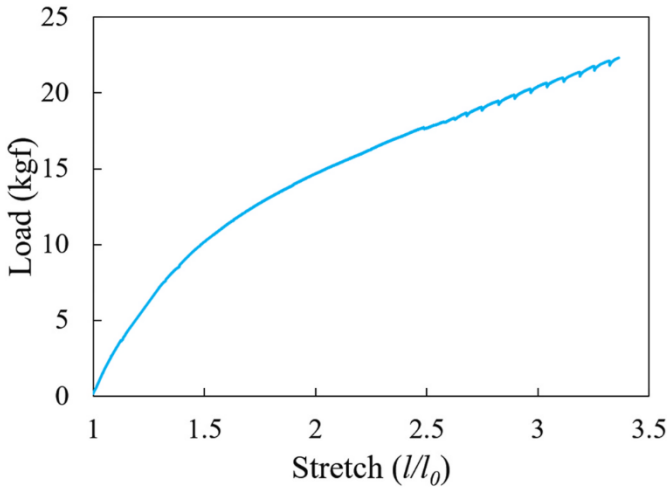

Fig. 5. The resulting load-stretch curve that features a softening behavior.

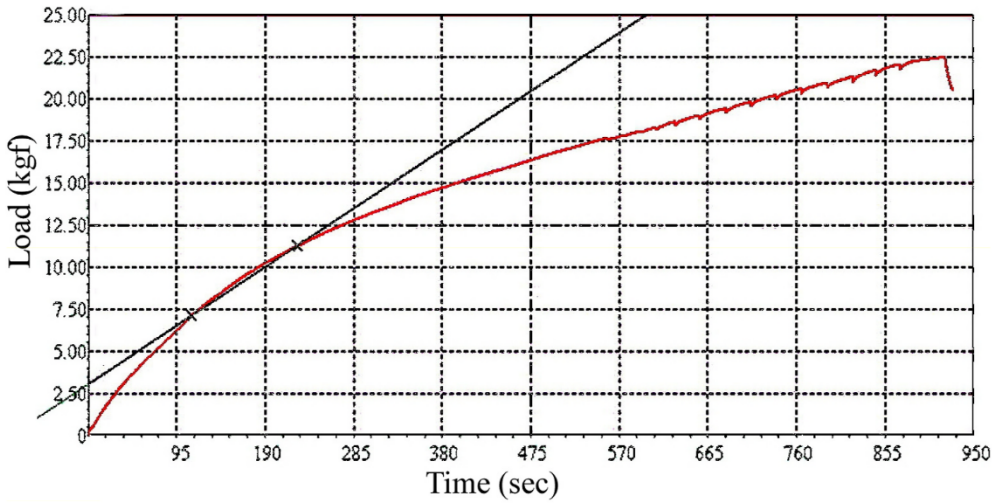

Fig. 4. The load histogram that is reported by the tensile testing machine.

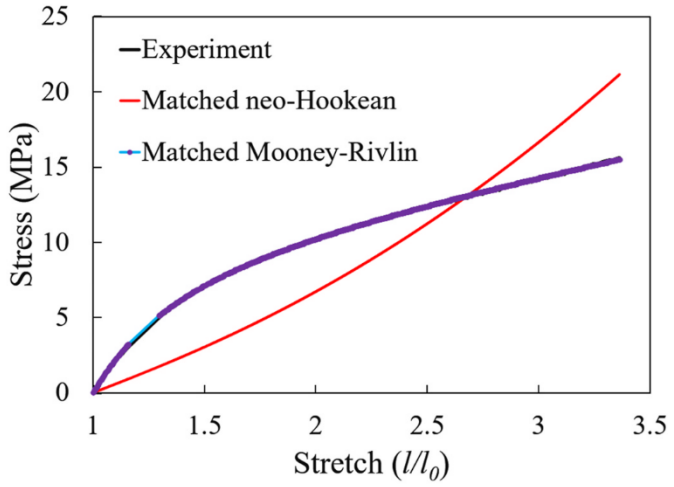

Fig. 6. A comparison among the matched neo-Hookean and Mooney-Rivlin hyperelastic models and the experimental 1D tensile results.

Table 2
The material constants associated with the matched neo-Hookean and Mooney-Rivlin hyperelastic models.

Neo-Hookean Model	Mooney-Rivlin Model	
C_1(MPa)	C_{01}(MPa)	C_{10}(MPa)
0.9598	3.315	1.478

l_0 and l are the initial and instantaneous gauge lengths, respectively. Eq. (42) represents a monotonically increase in the slope. For this reason, the relevant regression depicted in Fig. 6, indicates that the neo-Hookean model cannot accurately model the stretch-softening behavior of the material as it inherently implies a progressive stiffness (stiffening) behavior. In contrast, the Mooney-Rivlin has successfully captured the softening stress-stretch curve, due to including more polynomial terms, as Fig. 6 confirms. The material constants associated with the resulting regressions for the neo-Hookean and Mooney-Rivlin models are listed in Table 2. By exploring Fig. 5, one may deduce that while using the neo-Hookean model leads to erroneous results for the considered material, the Mooney-Rivlin curve is almost coincident with the real (experimental) stress-stretch curve of the material. For this reason, hereinafter, although the formulation of the neo-Hookean model has also been introduced in the previous sections and may be used for other materials, we proceed with the Mooney-Rivlin model only to ensure that the analytical results can be verified by the realistic/experimental results. The comparisons made by other researchers [37,38] emphasize the shortcomings of the neo-Hookean strain-energy density function in comparison to the Mooney-Rivlin strain-energy density expression.

Fig. 7. The employed DPI 610 Pneumatic Calibrator/Hand-Pump and the digital micrometer.

5.2. Experimental verification of the present results for an internally pressurized pipe/cylinder

In this connection, the mentioned PVC flexible clear water hose pipe/tube with inner and outer radii of 5 mm and 7 mm, respectively, was subjected to different internal pressures and the increase in the outer radius was measured. In this regard, one end of the tube was blocked and the air pressure was supplied by a DPI 610 Pneumatic Calibrator/Hand-Pump. This calibrator which is shown along with the high accuracy digital micrometer in Fig. 7, is a battery-powered package that contains a pressure generator, fine pressure control, device energizing, and output measurement. The produced internal pressure was varied in the range of 1 to 3.5 bar_g by steps of 0.5 bar_g. In each pressure, the tube was attached by glue at the contact line with the testing bed, in its final situation, to prevent its possible vertical and in-plane movements. Furthermore, to establish a plane-strain situation, the tube was kept straight during the test to avoid additional lateral/bending movements. The length of the tube was chosen to be 1 m, and both ends were fixed.

The increase in the outer radius was measured by an instrumentation calibration company utilizing two types of instrumentations, i.e., a dial indicator/gauge with a flat tip (for higher accuracy) and the digital micrometer as shown in Fig. 8 by accuracy in the order of 5 μm. The increases predicted for the outer radius by our formulation that is implemented to the Matlab computer code for various internal pressures are compared in Table 3 with the experimental ones.

5.3. The resulting distributions of the displacement and stress components along with the abaqus verifications

In addition to the displacement results, the stress results, and specifically, the predicted distributions of the displacement and stress components have to be verified as well. It is worth listing some of the superiorities of our *Point-Collocation-based Direct Hyperelasticity* Matlab computer code over the available commercial finite element analysis computer codes as:

a) Due to using an interlace formulation to compute the derivatives of the displacement components, the strain and stress components are continuous at the mutual boundaries of the adjacent discretization segments, in contrast to the commercial finite element analysis codes that use the C^0-continuous elements.
b) The present point collocation technique can capture the local variations of the quantities in contrast to the integral-based (i.e., finite element) method that distributes the local abrupt changes over the entire element domain. For this reason, the finite element method cannot capture the stress discontinuity/concentration exactly [27,39,40].
c) The assemblage of the equations of the discretization segments/elements takes place significantly easier than that of the finite element method.
d) The present governing equations of the hyperelastic cylinder differ from those of Abaqus. *Abaqus uses the energy method instead of directly solving the 3D hyperelasticity equations. In other words, the present formulation does not exist in Abaqus.*
e) In the commercial finite element analysis codes such as Abaqus, the incompressibility condition is fulfilled merely, by setting $J = 1$, but present formulation enforces this condition through calibrating the *hydrostatic* pressure with the pressure boundary conditions, in

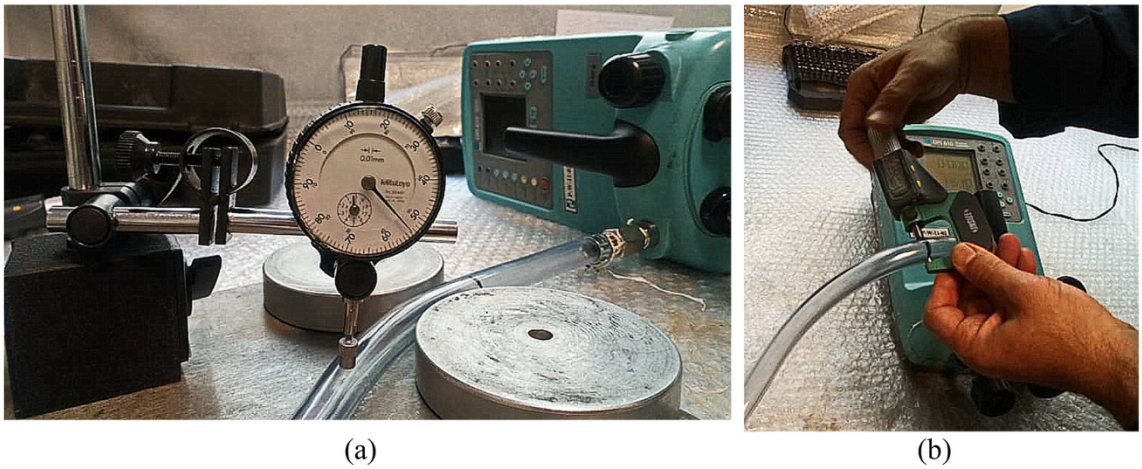

Fig. 8. The employed techniques for measurement of the increase in the outer radius of the tube.

Table 3
A comparison among present, Abaqus, and experimental results for the increase in the outer radius of the cylinder.

Magnitude of the internal pressure (bar)	Increase in the outer radius (mm)						
	Experimental	Abaqus		Discrepancy relative to the experimental (%)	Present		Discrepancy relative to the experimental (%)
		Raw	Up to 2 decimal places		Raw	Up to 2 decimal places	
1	0.04	0.03891	0.04	≅ 0	0.0383999	0.04	≅ 0
1.5	0.06	0.05901	0.06	≅ 0	0.0584486	0.06	≅ 0
2	0.08	0.07957	0.08	≅ 0	0.0788844	0.08	≅ 0
2.5	0.1	0.10060	0.10	≅ 0	0.0997227	0.10	≅ 0
3	0.12	0.12213	0.12	≅ 0	0.1209787	0.12	≅ 0
3.5	0.15	0.14416	0.14	6.7	0.1425713	0.14	6.7

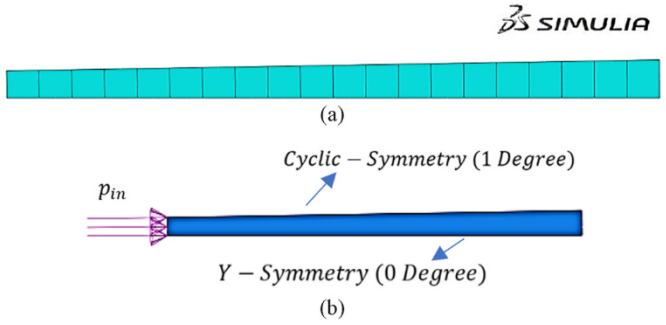

Fig. 9. (a) The mesh used in Abaqus and (b) the imposed restraints and load conditions.

addition to using the $J = 1$ condition. This hint/superiority has been achieved by using a penalty technique that enforces the pressure boundary condition by adding the displacement versions of the conditions appearing in Eqs. (32) and (33) by using a large multiplier, e.g., a 10^{10} coefficient.

Due to the axial symmetry of the loading and geometry of the cylinder and to use an efficient and computationally economic model, a sector of the cylinder with a central angle of 1° was chosen and discretized in the radial direction using the CPE8RH element. Adopting such a small angle prevents variations of the displacement and stress fields in the circumferential direction as well. The resulting mesh is shown in Fig. 9(a). Whilst the internal boundary of the meshed domain is subjected to the internal pressure, the top and bottom boundaries experience the symmetry conditions, i.e., the zero circumferential

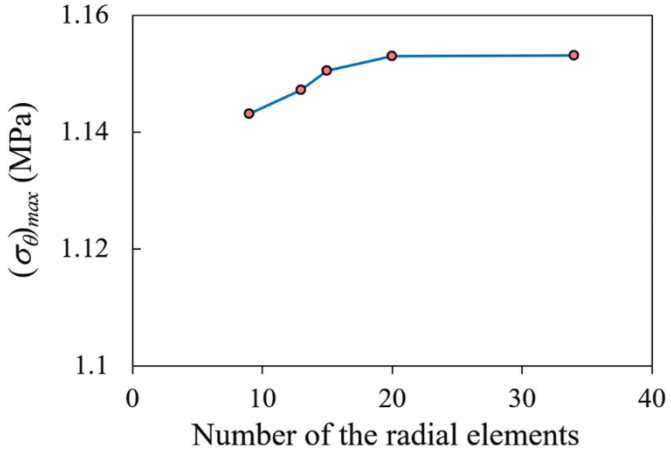

Fig. 10. Results of the convergence study regarding the number of the radial elements used in Abaqus.

displacements and zero slopes normal to the boundary (or zero in-plane shear stress). The boundary conditions are illustrated in Fig. 9(b).

A convergence study is performed to choose the appropriate number of elements in Abaqus. The material properties are identical to those found from the material properties identification experiments. As before, $a = 5$ mm, $b = 7$ mm. Fig. 10 illustrates the variations of the resulting maximum hoop stress that occurs at the inner boundary against the number of elements of the discretized domain. According to this figure, convergent results may be obtained by using 20 or a larger number of radial elements. A similar convergence study reveals that the

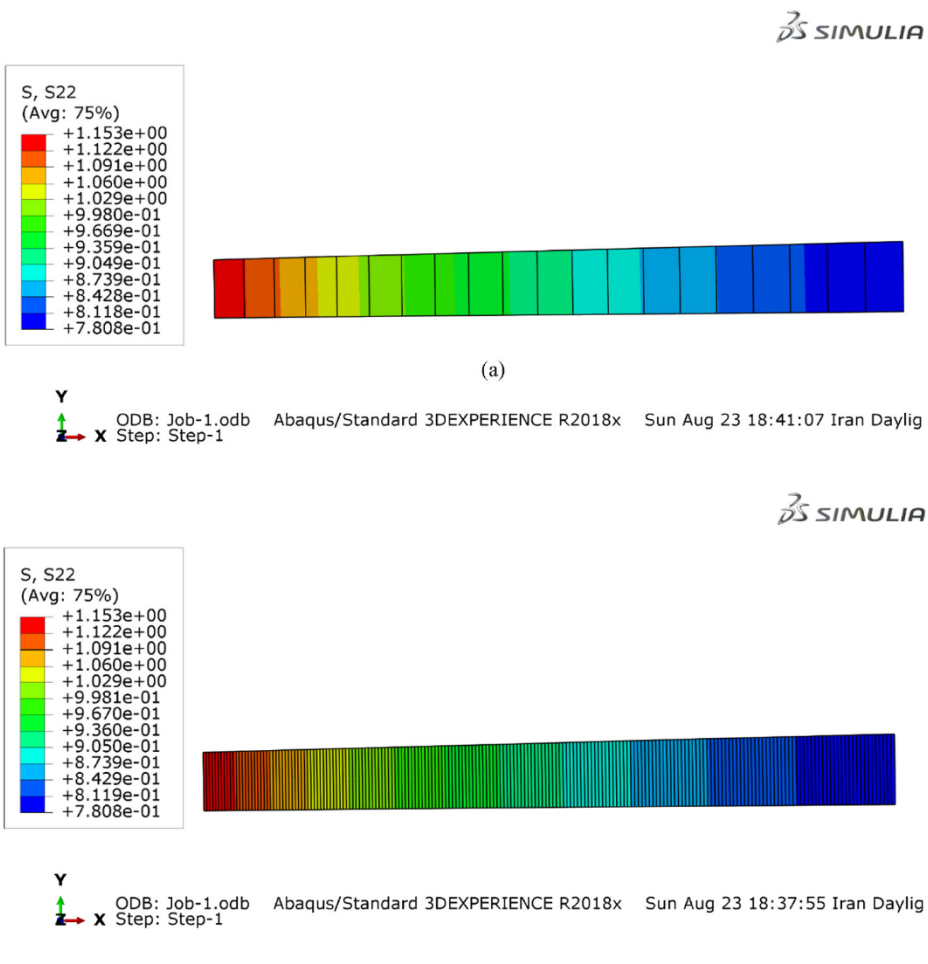

Fig. 11. The radial distributions of the hoop stress associated with (a) 20 and (b) 200 radial elements, for the highest considered internal pressure.

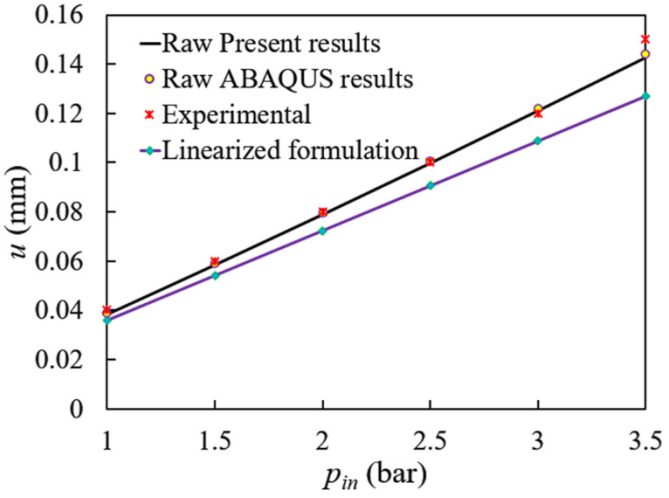

Fig. 12. A visual comparison among the present, Abaqus, and experimental results, for the increases in the outer radius, for the range of the internal pressures used in the experiment.

results of the present point collocation model are also convergent for *20 radial nodal points*. Choosing a higher number of elements leads to very negligible variations in the results. A comparison between the radial distributions of the hoop stress obtained for meshes with 20 and 200 radial elements in Abaqus is demonstrated in Fig. 11 for the highest employed pressure, confirms this claim.

As a first step, the present results of the increase in the outer radius of the cylinder are compared with the results of Abaqus in Table 3, in addition to the experimental results. As may be inferred from the results reported in Table 3, there is a good concordance between the results, for the full range of the internal pressure. To provide a clearer judgment, this comparison is presented visually in Fig. 12. Once again, the previous conclusion is confirmed. From the mathematical point of view, both our finite element analysis computer code and Abaqus results are extracted based on quadratic elements (in the radial direction). However, since the present point collocation method uses an interlace formulation that engages simultaneously the nodal values of the two adjacent elemental segments in computing the derivatives, in contrast to the finite element method that uses the internal nodal values of each element only, it seems that mathematically, the present formulation may establish a higher accuracy at the mutual boundaries of the radial segments. The stress components are related to derivatives of the displacement components through the constitutive law. Therefore, the stress components that are computed at the mutual boundary of the successive segments/elements based on derivatives of the displacement components that engage simultaneously the displacements of the two adjacent elements are continuous and mathematically more accurately than the those computed based on the procedure that is common in the finite element method (e.g. in Abaqus). In the latter procedure, each element uses its nodal displacements only in the determination of the derivatives of the displacement components and consequently, the determination of the

stress components. Therefore, the stress components computed for the adjacent elements may not be identical at their mutual boundaries.

Since the accuracy of the experimental measurement was up to 2 decimal places, the raw present and Abaqus results reported in Table 3 cannot be compared directly with the experimental results, due to the inherent round-off error in the experimental measurement. Instead, the present and Abaqus results have to be presented in numbers with up to 2 decimal places before the comparison. In such a way, one may see from Table 3 that the present computationally much economic algorithm leads to an accuracy that is identical to those of Abaqus.

To evaluate the simultaneous effects of the linearization of the constitutive law and the resulting system of equations, similar to those employed by Kiendl et al. [12] and Amabili et al. [15] on the results, a comparison is made with these simplified solutions as well in Fig. 12. As may be noted from Fig. 12, these simplifications have led to a kinematically stiffer structure, especially at larger loads. In the simplified analysis, the material properties were chosen according to the mid-point of the stress-stretch curve of the mentioned loading range (based on the non-simplified analysis results of the mid-layer). Although it may seem that the results vary linearly with the internal pressure, there are slight deviations from the linear behavior. This fact may be noted specifically when tracing variations of the experimental results in Fig. 12. The distribution of the radial deformation obtained in Abaqus is reported in

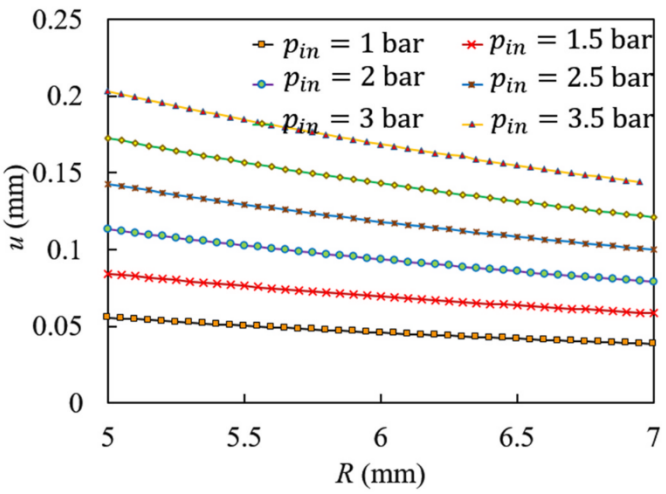

Fig. 14. The predicted radial deformation along the wall thickness of the Mooney-Rivlin hyperelastic cylinder, for various internal pressures.

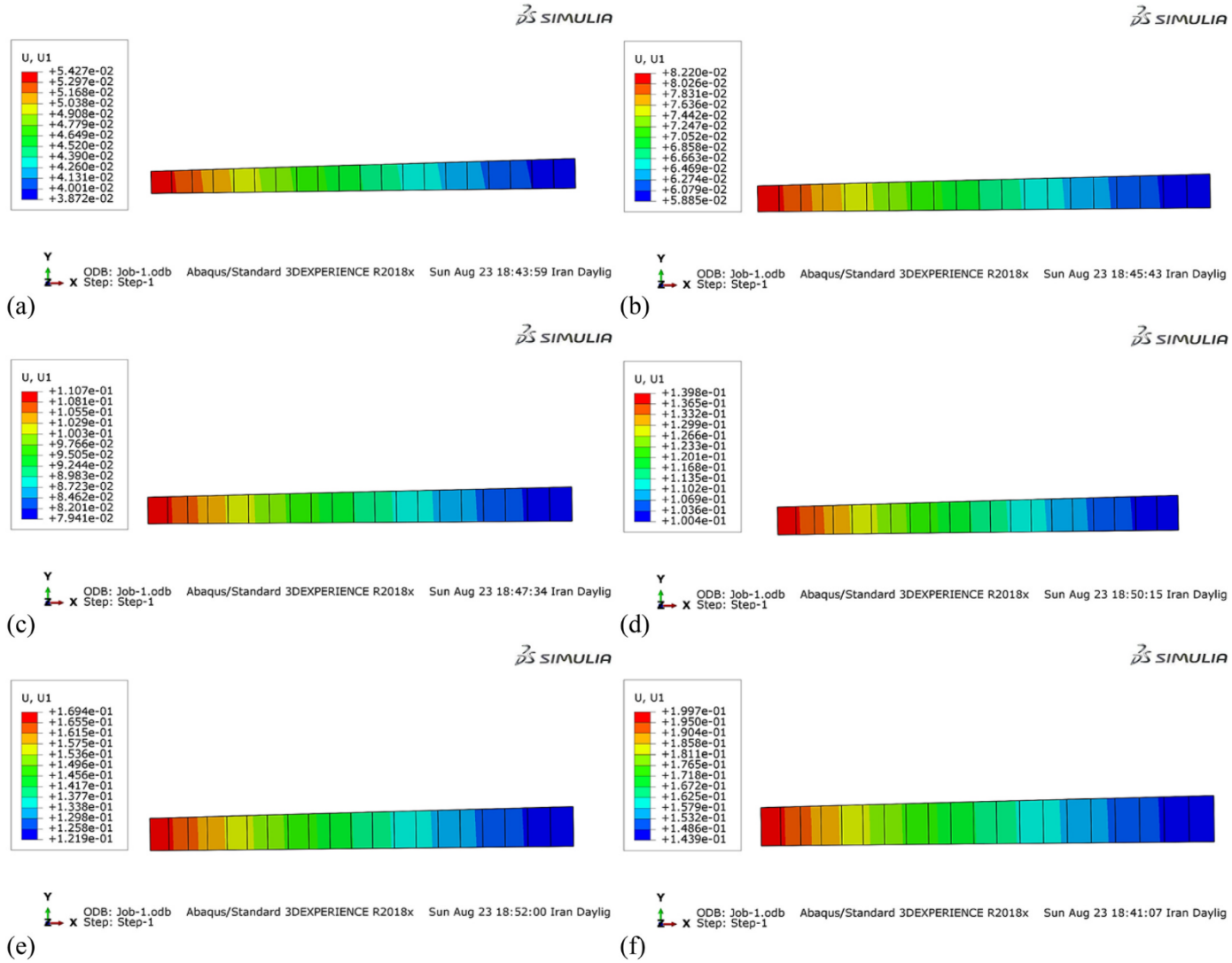

Fig. 13. The radial distribution of the radial displacement for various internal pressures: (a) $p_{in} = 1\ bar$, (b) $p_{in} = 1.5\ bar$, (c) $p_{in} = 2\ bar$, (d) $p_{in} = 2.5\ bar$, (e) $p_{in} = 3\ bar$, and (f) $p_{in} = 3.5\ bar$.

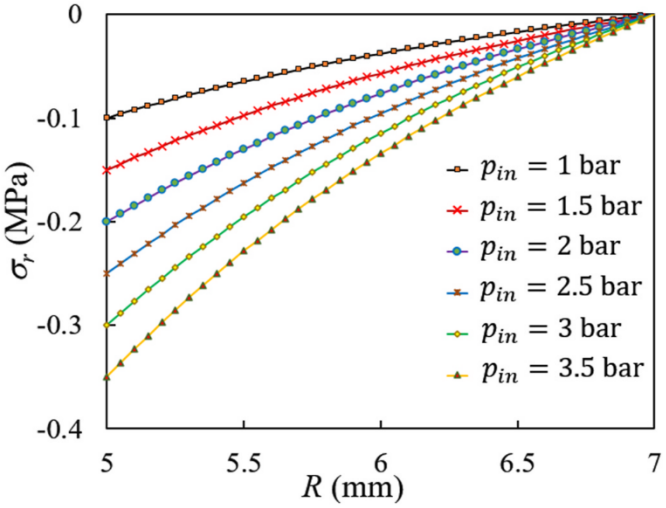

Fig. 15. The predicted radial stress along the wall thickness of the Mooney-Rivlin hyperelastic cylinder, for various internal pressures.

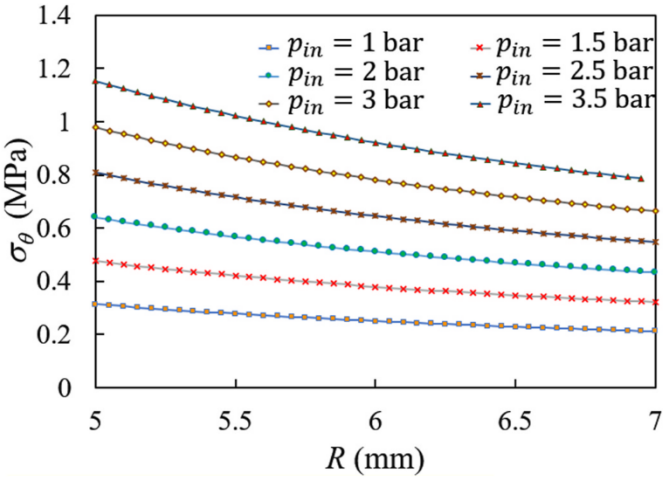

Fig. 16. The predicted hoop stress along the wall thickness of the Mooney-Rivlin hyperelastic cylinder, for various internal pressures.

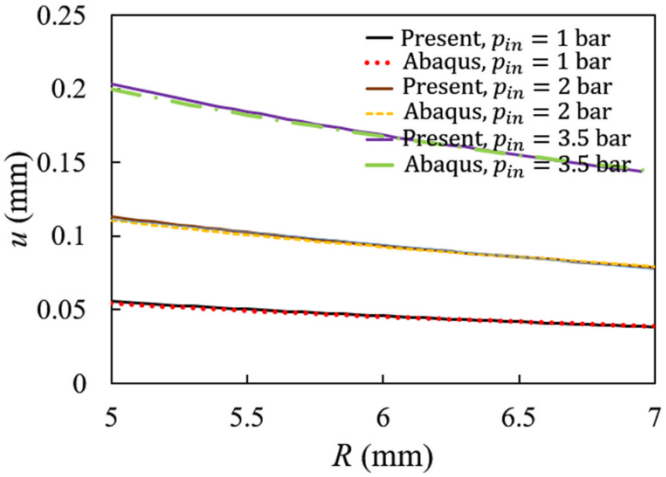

Fig. 17. A comparison between the present and Abaqus results for the radial deformation of the thick-walled Mooney-Rivlin hyperelastic cylinder, for various internal pressures.

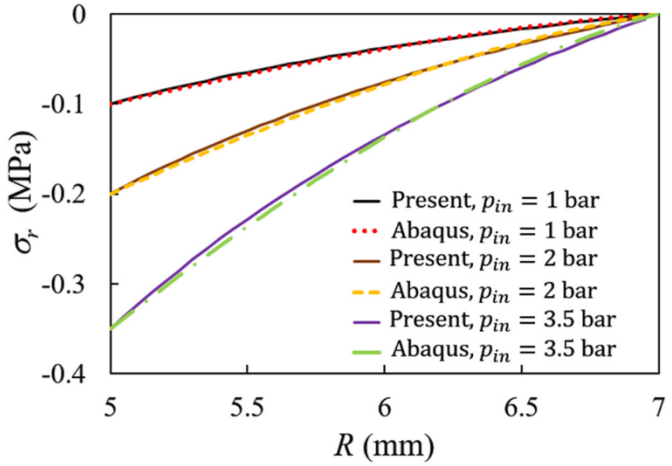

Fig. 18. A comparison between the present and Abaqus results for the radial stress of the thick-walled Mooney-Rivlin hyperelastic cylinder, for various internal pressures.

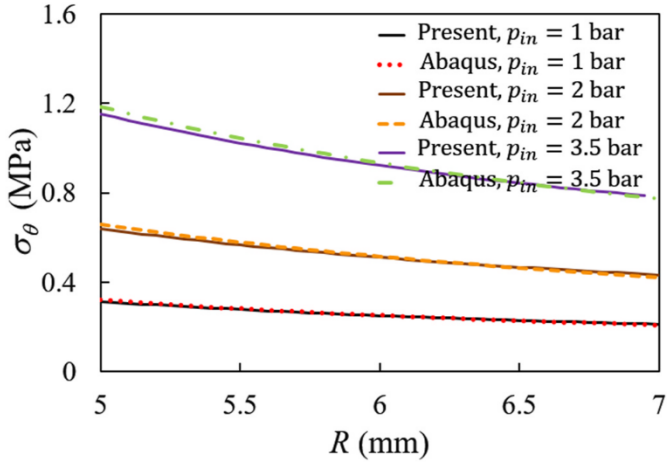

Fig. 19. A comparison between the present and Abaqus results for the hoop stress of the thick-walled Mooney-Rivlin hyperelastic cylinder, for various internal pressures.

Fig. 13.

The results demonstrated in Fig. 13 reveal that gradients of the radial displacement are larger in the neighborhood of the internal boundary of the cylinder.

Radial distributions of the radial displacement, radial stress, and circumferential stress of the hyperelastic cylinder are shown in Figs. 14–16, respectively, for different internal pressures. These figures show that gradients of variations of all the displacement and stress components are larger in the vicinity of the internal boundary. From Figs. 15 and 16 one may observe that in contrast to the internally pressurized elastic thick-walled cylinders, the $\sigma_r + \sigma_\theta$ expression is not constant throughout the thickness of the hyperelastic cylinder. This fact may readily be checked by computing the mentioned expression at the inner and outer layers. Furthermore, Figs. 14 and 16 reveal that the resulting radial displacement and circumferential stress, e.g., at the inner boundary, are not proportional to variations of the internal pressure of the cylinder.

The present radial distribution of the radial deformation and the radial and circumferential stresses are compared in Figs. 17–19, respectively. These results show an excellent agreement. The main origins of the discrepancy between the present and Abaqus results are:

(a) The nature of the employed solution technique. The present technique is a point collocation method that in addition to overcoming shortcoming of the stress jump at the mutual boundaries of the elements in Abaqus, provides extremely lower run times.
(b) The manner of imposing the incompressibility condition of the material. In Abaqus, this condition is fulfilled merely, by setting $J = 1$, but present formulation enforces this condition through calibrating the hydrostatic pressure with the pressure boundary conditions, in addition to imposing the $J = 1$ condition. This hint/superiority is made possible by using a penalty technique that enforces the pressure boundary condition by adding Eq (2). (32) and (33) by using a large multiplier, e.g., a 10^{10} coefficient.

Values of the radial stresses at the inner and outer boundaries confirm the accurately imposing of the boundary conditions.

6. Conclusions

In the present research, the distributions of the radial displacement, radial stress, and circumferential stress are studied for the internally pressurized thick-walled neo-Hookean and Mooney-Rivlin hyperelastic cylindrical pressure vessels/pipes. The theory of hyperelasticity, large-deformation strain-displacement expressions, and the incompressibility condition were employed to develop the second-order point-collocation analysis. No simplifications or linearization are made. Identification of the hyperelastic material properties and verification of the results are accomplished based on experiments conducted by the present authors. Since the present formulation is a direct application of the hyperelasticity theory and at the same time is quite new, it has not been included in any commercial finite analysis code (e.g., Abaqus) so far.

Some of the practical conclusions that may be drawn from the results section and the relevant discussions are:

- The neo-Hookean hyperelastic model represents a progressive stiffness model and thus, cannot be used for materials with stretch softening. On the contrary, due to having a larger number of terms, the Mooney-Rivlin model can be used for both stretch-softening and strain-hardening materials.
- The gradients of variations of all the displacement and stress components are larger in the vicinity of the internal boundary.
- In contrast to the internally pressurized elastic thick-walled cylinders, the $\sigma_r + \sigma_\theta$ expression is not constant throughout the thickness of the hyperelastic cylinder.
- Due to the nonlinear strain-displacement and constitutive relations, the resulting radial displacement and stress components are not proportional to variations of the internal pressure of the cylinder.
- The accuracy of the results of the employed 1D point-collocation technique is comparable to that of the 3D results of the commercial finite element analysis codes such as Abaqus. Instead, the present formulation and solution algorithm combination have the superiorities of higher stress continuity due to using interlaced discretization, the higher capability to capture the local variations due to its point-dependent rather than the integral-based (of the finite element method) nature, and employing a new formulation that utilizes the direct form of the hyperelasticity equilibrium equations rather than the energy method (that is used e.g., in Abaqus). Finally, the incompressibility condition is employed more accurately (in comparison to Abaqus) in the present research.

Author contribution

M. Shariyat: Conceptualization, Project administration, Supervision, Methodology, Validation, Formal analysis, Investigation, Data curation, Writing the English article, Visualization, Writing- Reviewing and Editing the responses to reviewers; M. Khosravi: Conceptualization, Methodology, Software and writing the Matlab code, Validation, Formal analysis, Investigation, Experimental data extraction, Data curation, Preparation of the original non-English draft, Contribution in writing the responses to reviewers; M. Yazdani Ariatapeh: Conceptualization, Methodology, Validation, Formal analysis, Investigation, Management of the experimental results extraction, Data curation, Preparation of the original non-English draft, Visualization; M. Najafipour: Methodology, Formal analysis, Conceptualization, Validation, Experimental data extraction, Visualization.

Declaration of competing interest

The authors declare that they have no known competing financial interests or personal relationships that could have appeared to influence the work reported in this paper.

Nomenclature

a	Inner radius of the cylinder
A	The right-hand side matrix
b	Outer radius of the cylinder
B	B_{ij} Left Cauchy-Green deformation tensor
C_1	Constant of neo-Hookean model
C_{10}, C_{01}	Constants of Mooney-Rivlin model
F, F_{ij}	The deformation gradient vector
i, j	Counters
I_1, I_2, I_3	Invariants of the left Cauchy-Green deformation tensor
$\bar{I}_1, \bar{I}_2$	Invariants of the strain tensor that do not change under pure volume change
J	Jacobian of the transformation
k	Stiffness matrix
K_1	Bulk modulus for small deformations
l_0, l	Initial and instantaneous gauge lengths
N	Number of the discretization segments
p	Hydrostatic pressure
p_{in}	Inner pressure
p_{out}	Outer pressure
r	Radial coordinate in the deformed configuration

R, R_i	Initial radial coordinate
S_{ij}	First Piola-Kirchhoff
u, u, u_i	Displacement components due to deformations
$W, \overline{W}$	Strain energy density
x_i	Original coordinates
X_j	Coordinates in the deformed geometry
z	Axial coordinate in the deformed configuration
Z	Initial axial coordinate
δ_{ij}	Kronecker's delta symbol
ε	Strain
θ	Circumferential coordinate in the deformed configuration
Θ	Initial circumferential coordinate
λ	Stretch
μ, μ_1, μ_2	Shear moduli for small deformations
σ_{ij}	Cauchy's stress components
$\sigma_{rr}, \sigma_{\theta\theta}$	Radial and circumferential stress components

References

[1] Z. Guo, J. Gattas, S. Wang, L. Li, F. Albermani, Experimental and numerical investigation of bulging behaviour of hyperelastic textured tubes, Int. J. Mech. Sci. 115–116 (2016) 665–675.
[2] R.M. Hackett, Hyperelasticity Primer, second ed., Springer, 2018.
[3] M. Shariyat, H. Ashrafi, H. Bandband, Brain tissue response analysis based on several hyperelastic models, for traumatic brain injury assessment, Universal Journal of Biomedical Engineering 4 (2016) 11–26.
[4] J.E. Mark, B. Erman, M. Roland, The Science and Technology of Rubber, Academic Press, 2013.
[5] B. Calvo, M.A. Martinez, M. Doblaré, On solving large strain hyperelastic problems with the natural element method, Int. J. Numer. Methods Eng. 62 (2005) 159–185.
[6] A.F. Bower, Applied Mechanics of Solids, CRC press, 2009.
[7] H. Altenbach, J. Pouget, M. Rousseau, B. Collet, T. Michelitsch (Eds.), Generalized Models and Non-classical Approaches in Complex Materials 2, Springer International Publishing, 2018.
[8] D.C. Pamplona, P.B. Goncalves, S.R. Lopes, Finite deformations of cylindrical membrane under internal pressure, Int. J. Mech. Sci. 48 (6) (2006) 683–696.
[9] R.M. Soares, P.F. Amaral, F.M. Silva, P.B. Gonçalves, Nonlinear breathing motions and instabilities of a pressure-loaded spherical hyperelastic membrane, Nonlinear Dynam. 99 (2020) 351–372.
[10] Y. Basar, Y. Ding, Finite-element analysis of hyperelastic thin shells with large strains, Comput. Mech. 18 (1996) 200–214.
[11] Y. Başar, Y. Ding, Shear deformation models for large-strain shell analysis, Int. J. Solid Struct. 34 (1997) 1687–1708.
[12] J. Kiendl, M.C. Hsu, M.C. Wu, A. Reali, Isogeometric Kirchhoff–Love shell formulations for general hyperelastic materials, Comput. Methods Appl. Mech. Eng. 291 (2015) 280–303.
[13] K. Luo, C. Liu, Q. Tian, H. Hu, Nonlinear static and dynamic analysis of hyper-elastic thin shells via the absolute nodal coordinate formulation, Nonlinear Dynam. 85 (2016) 949–971.
[14] I.D. Breslavsky, M. Amabili, M. Legrand, Static and dynamic behavior of circular cylindrical shell made of hyperelastic arterial material, J. Appl. Mech. 83 (5) (2016), 051002.
[15] M. Amabili, I.D. Breslavsky, J.N. Reddy, Nonlinear higher-order shell theory for incompressible biological hyperelastic materials, Comput. Methods Appl. Mech. Eng. 346 (2019) 841–861.
[16] J. Zhang, J. Xu, X. Yuan, H. Ding, D. Niu, W. Zhang, Nonlinear vibration analyses of cylindrical shells composed of hyperelastic materials, Acta Mech. Solida Sin. 32 (4) (2019) 463–482.
[17] S.S. Mirjavadi, M. Forsat, S. Badnava, Nonlinear modeling and dynamic analysis of bioengineering hyper-elastic tubes based on different material models, Biomech. Model. Mechanobiol. (2019), https://doi.org/10.1007/s10237-019-01265-8.
[18] K. Arya, S. Sarangi, R. Bhattacharyya, A damaged Ogden material tube under pressure: stability and bifurcation analysis, Soft Mater. 18 (2020) 74–88.
[19] N. Roussos, D.P. Mason, D.L. Hill, On non-linear radial oscillations of an incompressible, hyperelastic spherical shell, Math. Mech. Solid 7 (2002) 67–85.
[20] J.S. Ren, Dynamical response of hyper-elastic cylindrical shells under periodic load, Appl. Math. Mech. 29 (2008) 1319.
[21] R.C. Batra, A. Bahrami, Inflation and eversion of functionally graded non-linear elastic incompressible circular cylinders, Int. J. Non Lin. Mech. 44 (2009) 311–323.
[22] A. Almasi, M. Baghani, A. Moallemi, Thermomechanical analysis of hyperelastic thick-walled cylindrical pressure vessels, analytical solutions and FEM, Int. J. Mech. Sci. 130 (2017) 426–436.
[23] A. Almasi, M. Baghani, A. Moallemi, M. Baniassadi, G. Faraji, Investigation on thermal stresses in FGM hyperelastic thick-walled cylinders, J. Therm. Stresses 41 (2018) 204–221.
[24] D. Aranda-Iglesias, J.A. Rodríguez-Martínez, M.B. Rubin, Nonlinear axisymmetric vibrations of a hyperelastic orthotropic cylinder, Int. J. Non Lin. Mech. 99 (2018) 131–143.
[25] M.H. Ghadiri Rad, F. Shahabian, S.M. Hosseini, Geometrically nonlinear elastodynamic analysis of hyper-elastic neo-Hooken FG cylinder subjected to shock loading using MLPG method, Eng. Anal. Bound. Elem. 50 (2015) 83–96.
[26] A. Bagheri, D. Taghizadeh, H. Darijani, On the behavior of rotating thick-walled cylinders made of hyperelastic materials, Meccanica 51 (2016) 673–692.
[27] M. Shariyat, M.R. Eslami, Isoparametric finite-element thermoelasto-plastic creep analysis of shells of revolution, Int. J. Pres. Ves. Pip. 68 (1996) 249–259.
[28] M. Shariyat, S.M.H. Lavasani, M. Khaghani, Nonlinear transient thermal stress and elastic wave propagation analyses of thick temperature-dependent FGM cylinders, using a second-order point-collocation method, Appl. Math. Model. 34 (2010) 898–918.
[29] M. Shariyat, M. Ghafourinam, Hygrothermomechanical creep and stress redistribution analysis of thick-walled FGM spheres with temperature and moisture dependent material properties and inelastic radius changes, Int. J. Pres. Ves. Pip. 169 (2019) 94–114.
[30] M. Shariyat, A nonlinear Hermitian transfinite element method for transient behavior analysis of hollow functionally graded cylinders with temperature-dependent materials under thermo-mechanical loads, Int. J. Pres. Ves. Pip. 86 (2009) 280–289.
[31] M. Shariyat, S. Jahanshahi, H. Rahimi, Nonlinear Hermitian generalized hygrothermoelastic stress and wave propagation analyses of thick FGM spheres exhibiting temperature, moisture, and strain-rate material dependencies, Compos. Struct. 229 (2019) 111364.
[32] M. Shariyat, R. Mohammadjani, Three-dimensional stress field analysis of rotating thick bidirectional functionally graded axisymmetric annular plates with nonuniform loads and elastic foundations, J. Compos. Mater. 48 (2014) 2879–2904.
[33] M. Shariyat, R. Mohammadjani, Three-dimensional dynamic stress and vibration analyses of thick singular-kernel fractional-order viscoelastic annular rotating discs under nonuniform loads, Int. J. Struct. Stabil. Dynam. 20 (2020), 2050007.
[34] M. Shariyat, R. Mohammadjani, 3D nonlinear variable strain-rate-dependent-order fractional thermoviscoelastic dynamic stress investigation and vibration of thick transversely graded rotating annular plates/discs, Appl. Math. Model. 84 (2020) 287–323.
[35] T.R. Chandrupatla, A.D. Belegundu, Introduction to Finite Elements in Engineering, fourth ed., Pearson Education Limited, 2011.
[36] ASTM International, Designation: D638-14- Standard Test Method for Tensile Properties of Plastics, vol. 82, ASTM, 2014, pp. 1–17.
[37] P. Tejasri, A. Basak, Comparative study of computational material models, Int. J. Appl. Eng. Res. 13 (2018) 8588–8595.
[38] G. Marckmann, E. Verron, Comparison of hyperelastic models for rubber-like materials, Rubber Chemistry and Technology 79 (2006) 835–858.
[39] P.L. Gould, Finite Element Analysis of Shells of Revolution, Pitman Publishing, New York, NY, U.S.A., 1985.
[40] O.C. Zienkiewicz, R.L. Taylor, D.D. Fox, The Finite Element Method for Solid and Structural Mechanics, seventh ed., Butterworth-Heinemann, Elsevier, Oxford, 2014.